

The Solar Electron and Proton Telescope for the STEREO Mission

R. Müller-Mellin · S. Böttcher · J. Falenski · E. Rode ·
L. Duvet · T. Sanderson · B. Butler · B. Johlander ·
H. Smit

Received: 26 June 2006 / Accepted: 27 April 2007
© Springer Science+Business Media B.V. 2007

Abstract The Solar Electron and Proton Telescope (SEPT), one of four instruments of the Solar Energetic Particle (SEP) suite for the IMPACT investigation, is designed to provide the three-dimensional distribution of energetic electrons and protons with good energy and time resolution. This knowledge is essential for characterizing the dynamic behaviour of CME associated and solar flare associated events. SEPT consists of two dual double-ended magnet/foil particle telescopes which cleanly separate and measure electrons in the energy range from 30–400 keV and protons from 60–7 000 keV. Anisotropy information on a non-spinning spacecraft is provided by the two separate telescopes: SEPT-E looking in the ecliptic plane along the Parker spiral magnetic field both towards and away from the Sun, and SEPT-NS looking vertical to the ecliptic plane towards North and South. The dual set-up refers to two adjacent sensor apertures for each of the four view directions: one for protons, one for electrons. The double-ended set-up refers to the detector stack with view cones in two opposite directions: one side (electron side) is covered by a thin foil, the other side (proton side) is surrounded by a magnet. The thin foil leaves the electron spectrum essentially unchanged but stops low energy protons. The magnet sweeps away electrons but lets ions pass. The total geometry factor for electrons and protons is $0.52 \text{ cm}^2 \text{ sr}$ and $0.68 \text{ cm}^2 \text{ sr}$, respectively. This paper describes the design and calibration of SEPT as well as the scientific objectives that the instrument will address.

Keywords Solar energetic particles · CME · Acceleration · Propagation · Instrumentation

1 Introduction

The twin observatories of the STEREO mission will perform comprehensive studies of Coronal Mass Ejections (CMEs) directed towards Earth from two vantage points which

R. Müller-Mellin (✉) · S. Böttcher · J. Falenski · E. Rode
Universität Kiel, 24118 Kiel, Germany
e-mail: mueller-mellin@physik.uni-kiel.de

L. Duvet · T. Sanderson · B. Butler · B. Johlander · H. Smit
ESA/ESTEC, 2200 Noordwijk, The Netherlands

allow stereoscopic remote observations of CMEs and multi-point in-situ measurements of their interplanetary counterparts (ICMEs). The angle STEREO-A–Sun–STEREO-B increases at a rate of 44 degrees per year. As the observatories separate, larger ICME structures are revealed by the particles and field instruments of the IMPACT investigation. When the Sun transforms stored magnetic energy into electromagnetic radiation and kinetic energy of coronal matter (increased bulk motion of plasma as well as acceleration of energetic particles) the solar energetic particles (SEPs) bear the imprint of the various physical processes at work and of the regions through which they have travelled. Examples of these processes are stochastic acceleration, involving resonant wave–particle interactions that transfer energy from waves to particles or shock acceleration where resonant wave generation by particles traps them near the shock increasing the efficiency of their acceleration to higher energies. Electrons and protons are a major contributor to the energy balance and dynamics of the interplanetary medium. They outnumber by far the remaining constituents of the particle population. A considerable amount of the total energy release during a CME can be imparted to energetic particles in the energy interval 10 keV to 1 GeV, whereof up to 80% can be accounted for by protons and up to 18% by electrons (Mewaldt et al. 2005). Their greatly differing mass can uniquely reveal the details of acceleration and propagation mechanisms. Solar flare or shock accelerated electrons reach the Earth rapidly compared to protons assuming a simultaneous release at the Sun (Klein and Posner 2005). Their energy spectra will be useful as predictors of the severity of terrestrial effects.

The Solar Electron and Proton Telescope (SEPT) is one of seven instruments of the IMPACT investigation and is designed to cleanly separate and measure electrons in the energy range from 30–400 keV and protons from 60–7 000 keV. The electron measurements will cover the gap with some overlap between suprathermal electrons measured by STE (Luhmann et al. 2007) and high energy electrons measured by HET (von Rosenvinge et al. 2007). The proton measurements fill in without completely covering the gap between solar wind energies (PLASTIC SWS; Galvin et al. 2007) and higher energy measurements of LET (2–13 MeV; Mewaldt et al. 2007) as well as HET (13–100 MeV). The four SEPT instruments for the twin STEREO mission are shown in Fig. 1, their essential features are summarized in Table 1. A discussion of the scientific objectives is presented in Sect. 2, while details of the design and calibration can be found in Sects. 3 and 4.

2 Science Objectives

2.1 SEP Acceleration

Energetic processes on the Sun are known to occasionally accelerate protons to GeV and electrons to tens of MeV energies. First evidence of high-energy particles from the Sun was obtained 60 years ago when Forbush studied the large solar events of February and March of 1942 (Forbush 1946). Since then extensive knowledge of energy spectra, abundance variations, intensity-time profiles, and spatial distributions has been gathered leading in the 1980s to the classification of solar energetic particle events into gradual events—accelerated by shock waves driven outward by coronal mass ejections—and impulsive events originating from a stochastic acceleration process in the flare site (Cane et al. 1986; Reames 1995). However, in recent years several studies have challenged this classification. In a refinement of the two-class picture (Cliver 1996) it was suggested that gradual events possess an impulsive “core” in which similar acceleration processes as in impulsive flares operate, and from which particles can escape into the interplanetary medium where they can be observed

Fig. 1 SEPT-E (*in front*) and SEPT-NS (*on bracket*). SEPT for Ahead S/C with doors closed (*right*), and for Behind S/C with doors open (*left*)



Table 1 Summary of SEPT characteristics

Characteristic	Value	Details
Measurement objective	Clean separation of electrons and protons and measurement of their energy spectra and angular distribution	Sect. 2
Measurement technique	Total energy measurement in magnet/foil particle telescope	Sect. 3.1.2
Sensor system	Ion-implanted Si detectors (300 μm thick) in anti-coincidence configuration. Rare-Earth magnets (remanence 0.5 tesla in the air gap) to deflect electrons. Parylene foil (4.95 μm thick) to stop protons.	Sects. 3.1.3, 3.1.4, 3.1.5
Energy interval		Sect. 4
Electrons	30–400 keV	
Protons	60–7 000 keV	
Field of view		Sect. 3.1.2
Electrons	$4 \times 52.8^\circ$ conical	
Protons	$4 \times 52.0^\circ$ conical	
Geometrical factor		Sect. 3.1.2
Electrons	$4 \times 0.13 \text{ cm}^2 \text{ sr}$	
Protons	$4 \times 0.17 \text{ cm}^2 \text{ sr}$	
Resources	SEPT-E	SEPT-NS with bracket
Dimensions	$99 \times 156 \times 147 \text{ mm}^3$	$100 \times 175 \times 312 \text{ mm}^3$
Mass	795 g	1175 g
Power (worst case)	600 (765) mW	600 (765) mW
Bit rate (beacon)	40 (3) bit/s	40 (3) bit/s

together with particles accelerated by a CME-driven shock (for a review see Reames 1999; Kallenrode 2003). The existence of these “hybrid” cases poses a challenge to the observer to characterize and identify “pure” events which best allow studies of the two acceleration mechanisms.

SEPT will use near-relativistic electrons as time markers for injection of solar particles. The onset times of these escaping electrons can be compared to electromagnetic radiation signatures of interacting particles and dispersion-dependent arrival times of escaping protons. Time variations, energy spectra and angular distributions will be studied to answer important questions like:

- (1) Are particles which are accelerated in the low and middle corona prevented from travelling to Earth either by the CME shock (Kahler 1996) or because they are supposedly trapped in the coronal magnetic fields (Reames 2002)?
- (2) If these particles contribute to CME-associated SEP events, is their escape energy-dependent?
- (3) Are there different acceleration sites for interacting and escaping particles?
- (4) While the shock wave may continue to accelerate particles all the way from the solar corona to beyond 1 AU, are there identifiable contributions from particles well behind the front of the CME at the time of acceleration (Klein and Posner 2005)?
- (5) Representing the measured electron and proton spectra by a power law modulated by an exponential, can we distinguish whether the spectra are dominated by acceleration effects or transport effects?
- (6) Can we distinguish signatures of solar injection from in-situ acceleration processes?

2.2 Comparing Gradual and Impulsive SEP Events

Historically the terms impulsive and gradual were introduced to describe soft X-ray events on the Sun to which SEP events could later be associated. While the X-ray time scales “impulsive vs. gradual” only poorly resolve the acceleration mechanism, impulsive particle events can be distinguished from gradual events by their elemental and isotope abundances, ionization states, energy spectra, angular distributions and time behaviour (Reames 1999). They are electron rich, and their proton to helium ratio is low (Mueller-Mellin et al. 1993), their Fe charge state is high (Luhn et al. 1987; Tylka et al. 1995), and they are rich in ^3He and enhanced in heavy elements up to Fe (Reames 1988). Table 2 summarizes these particle characteristics which reflect the paradigm as of the early 1990’s. As stated in Sect. 2.1, refined measurement techniques have been applied in solar cycle 23 which modify this picture. Thus, most gradual events include ^3He in excess of the solar wind ratio (Cohen et al. 1999; Mason et al. 1999). Also the Fe charge states and the Fe/O ratio can vary considerably from event to event in both impulsive and gradual events, and the Fe charge state is found to be energy dependent, ranging from ~ 10 to 20 (Moebius et al. 2003; Klecker et al. 2006). The scheme in Table 2 serves to classify the particle signatures in comparison to electromagnetic properties of Table 3 even if SEPT cannot contribute to charge state or composition measurements other than electron/proton ratios and even if mixed events are known to be a common feature.

Solar energetic electron and ion observations often correlate with solar radio and optical observations. The properties of electromagnetic radiation of impulsive and gradual flares which can be associated with SEP events are given in Table 3. The complement of remote and in-situ instrumentation onboard STEREO will greatly support correlation studies with SEPT data to understand the physical processes of the active Sun and in the disturbed interplanetary medium.

Table 2 Classes of solar particle events

	Gradual	Impulsive
Particles	Proton rich	Electron rich
$^3\text{He}/^4\text{He}$	~ 0.0005	~ 1
Fe/O	~ 0.15	~ 1.2
H/He	~ 100	~ 10
Q_{Fe}	~ 14	~ 20
Duration	Days	Hours
Longitude distribution	$\leq 180^\circ$	$< 30^\circ$
Solar wind signature	Interplanetary shock	–
Event rate	~ 10 per year	1000 per year

Table 3 Electromagnetic properties of gradual and impulsive flares (Kallenrode 2003)

	Gradual	Impulsive
Duration in soft X-rays	> 1 h	< 1 h
Decay in soft X-rays	> 10 min	< 10 min
Duration in hard X-rays	> 10 min	< 10 min
Duration in microwaves	> 5 min	< 5 min
Metric type II	Always	75%
Metric type III	50%	Always
Metric type IV	Always	Rare
Chromospheric $\text{H}\alpha$ size	Large	Small
Height in corona	$\sim 5 \times 10^4$ km	$\leq 10^4$ km
Volume	$10^{28} - 10^{29} \text{ cm}^3$	$10^{26} - 10^{27} \text{ cm}^3$
Energy density	Low	High
Coronal mass ejections	Always	Rare

2.3 ICME Topology

Magnetic clouds are often embedded in ICMEs (interplanetary evolution of a CME). It is known that electrons of 100 eV to 1 keV streaming out from the hot tail of the coronal thermal distribution become bidirectional if they enter magnetic clouds where both ends intercept the corona (Gosling et al. 1987). But also electrons and ions in the SEPT energy range can lend support in outlining the ICME topology when their counterstreaming is observed. Anisotropy information on the non-spinning STEREO spacecraft is provided by the two separate telescopes: SEPT-E looking in the ecliptic plane along the Parker spiral magnetic field both towards and away from the Sun, and SEPT-NS looking vertical to the ecliptic plane towards North and South. The answers to questions of how the field lines are routed inside an ICME or whether the field lines in an ICME are still connected to the Sun as opposed to a detached plasmoid can find further corroboration by measurements of the angular distribution.

2.4 Space Weather

Electrons from SEP events reach the Earth rapidly, carrying significant information about the source region. In particular, electrons from flare sites produce hard spectra which almost

never produce effects on the Earth's magnetosphere and atmosphere. Conversely, shock accelerated electrons are associated with proton-rich SEP events signalling the arrival of stormy conditions with the power to imperil satellites, take down power grids, disrupt communications, pose a radiation hazard to astronauts, or produce colourful aurorae. However, there are statistical studies (Oakley et al. 2003) which claim a correlation of radio type II bursts with hard electron spectra. When properly understood, electron spectra and the electron to proton ratio will be useful as predictors of the severity of terrestrial effects. SEPT data are included in the IMPACT beacon mode data set for continuous transmission to the ground stations. Four energy bands for electrons and four energy bands for protons are provided with a time resolution of one minute. The lowest and highest energy bands are sectorized in four directions.

3 Instrument Description

3.1 Approach

3.1.1 Design Requirements

Providing the three-dimensional distribution of energetic electrons and protons with good energy resolution poses several instrumental challenges: as singly charged particles in the energy range from some 10 keV to several MeV deposit only small amounts of energy in a solid state detector, the requirements on noise suppression are more stringent than they would be for heavier ions. Furthermore, separating electrons from protons in this energy range is complicated by the fact that the well-proven $dE/dx - E$ approach is not viable as it is for higher energies because one cannot afford to have two measurements in separate detectors: either the dE/dx detector would stop all the low energy particles before they reach the E detector or the dE/dx detector would have to be made so thin as to render the signal of a penetrating singly-charged particle indiscernible from detector noise. In addition the spectra of solar energetic particles have a steep spectral slope, i.e. an instrument has to cope with very high fluxes at low energies. Also, as the spacecraft is not spinning, special efforts must be made to acquire anisotropy information. Finally, the secondary particles generated by solar and galactic cosmic rays in the surrounding matter of the spacecraft constitute a background against which good discrimination is mandatory. The following discussion will document how these requirements were met.

3.1.2 The Detector System

Each double-ended telescope has two solid state detectors (SSDs) which are operated in anti-coincidence. One SSD looks through an absorption foil and its partner through the air gap of a magnet system. The foil leaves the electron spectrum essentially unchanged but stops protons of energy up to the energy of electrons (~ 400 keV) which penetrate the SSD. The magnet is designed to sweep away electrons below 400 keV, but leaves ions unaffected. In the absence of >400 keV ions, the foil SSD only detects electrons, and the magnet SSD only detects ions. Ions from 400 keV to 7 MeV will stop in the magnet SSD and their fluxes will be cleanly measured. The contribution of >400 keV ions to the foil SSD can then be computed and subtracted to obtain the electron fluxes. The SEPT sensor schematics are shown in Fig. 2. Some SEPT sensor characteristics are given in Table 4.

Table 4 SEPT sensor characteristics

Channel (anti) coinc.	Particle species	Geometrical factor	View cone	Boresight ahead S/C	Accum. time
D0 D1 G0 G1	electrons 30–480 keV	0.13 cm ² sr	52.8°	ecliptic 135°	60 s
D1 D0 G0 G1	protons 70–6 500 keV	0.17 cm ² sr	52.0°	ecliptic 315°	60 s
D2 D3 G2 G3	electrons 30–480 keV	0.13 cm ² sr	52.8°	ecliptic 315°	60 s
D3 D2 G2 G3	protons 70–6 500 keV	0.17 cm ² sr	52.0°	ecliptic 135°	60 s
D4 D5 G4 G5	electrons 30–480 keV	0.13 cm ² sr	52.8°	north	60 s
D5 D4 G4 G5	protons 70–6 500 keV	0.17 cm ² sr	52.0°	south	60 s
D6 D7 G6 G7	electrons 30–480 keV	0.13 cm ² sr	52.8°	south	60 s
D7 D6 G6 G7	protons 70–6 500 keV	0.17 cm ² sr	52.0°	north	60 s

Note: Channels of SEPT-E and -NS on Behind S/C with reversed boresight

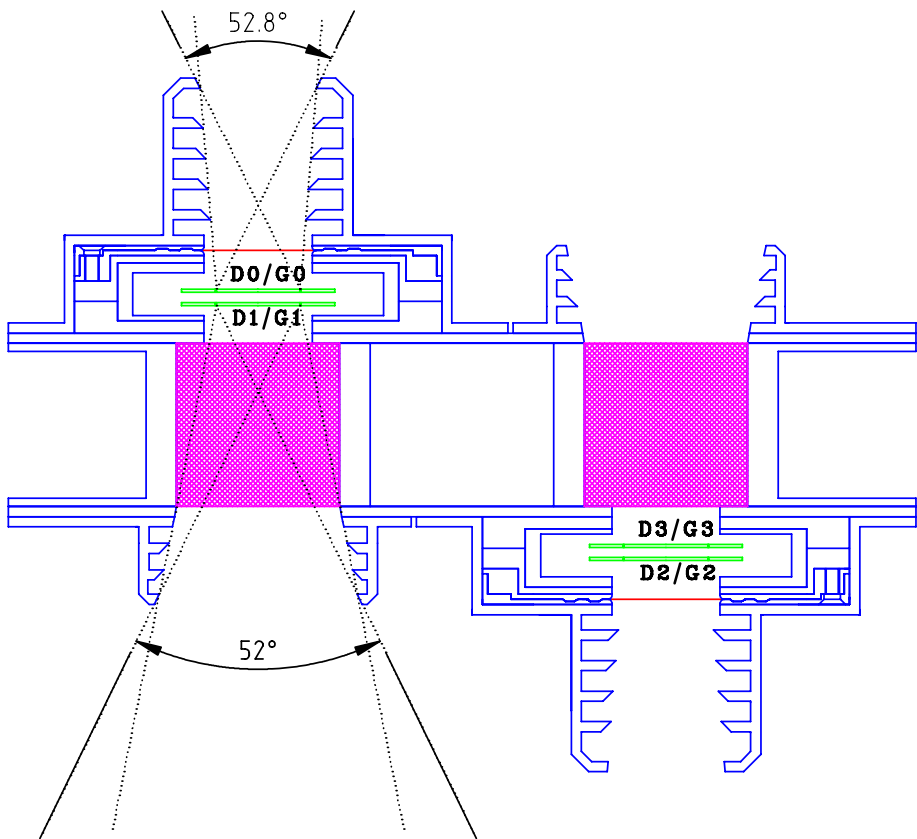


Fig. 2 SEPT sensor schematics. Detection elements are silicon detectors (D0, . . . , D3, green) with guard rings (G0, . . . , G3), Parylene foils (red), and magnetic fields perpendicular to the drawing plane (magenta)

Anisotropy information is acquired in four look directions: SEPT-E observes in the ecliptic plane along the nominal Parker spiral magnetic field direction both forward and backward, SEPT-N/S observes out of the ecliptic plane perpendicular to the magnetic field both

Table 5 PIPS specification

Detector active area	center: 53 mm ² , ring 58 mm ²
Detector diameter	center: 8.2 mm, ring: 12 mm crosstalk ring: 8.4 mm
Chip dimensions	flat to flat: 15.15 mm on diagonal: 16.4 mm
Chip thickness	300 ± 25 µm
Depletion depth (min./max.)	285/325 µm
Contact to junction	wire bonding
Contact to ohmic side	wire bonding
Junction window thickness	< 1 500 nm
Ohmic window thickness	< 350 nm
Detector capacitance	center: 20 pF, ring 21 pF
Nominal operating voltage	40 V
Actual operating voltage	80 V
Current at 20°C at 5 000 lux	typ. 15 nA, max. 60 nA

North and South. Thus, SEPT partially complements the viewing directions for ions of the Low Energy Telescope (LET, see Mewaldt et al. 2007) the multiple look directions of which are all in the ecliptic. To warrant unobstructed fields of view, the full angle of the viewing cones is limited to 52 degrees and SEPT-N/S is mounted on its own mounting bracket. The geometrical factor for each of the four magnet telescopes is 0.17 cm² sr and for each of the four foil telescopes 0.13 cm² sr.

3.1.3 The Solid State Detectors

The SSDs are of the Passivated Ion-implanted Planar Silicon (PIPS) type. Each SSD is surrounded by an active guard ring on the same Si wafer and closely stacked with its partner at 1 mm separation. To achieve low background, the output of each center segment is operated in anti-coincidence with its own guard ring and with its partner and the partner's guard ring to reject penetrating particles or secondary particles from outside the viewing cone. A special feature is the implementation of a 100 µm wide crosstalk ring between center segment and guard ring to prevent a veto by crosstalk for large pulses. The detector specifications are given in Table 5. Figure 3 shows the detector layout with three solder pads for center segment, guard ring, and crosstalk ring. As some detectors will see stray light from minor impingements of antennas and solar panels in their fields of view, all detectors are mounted with their ohmic side facing outward, which is treated with a 170 nm aluminium layer for light tightness. Each detector is biased at least 50 V beyond its depletion voltage to account for radiation dose effects towards the end of mission life time. The PIPS detectors are manufactured by Eurisys Canberra, Belgium.

3.1.4 The Magnet System

The magnet system consists of four rare-earth permanent magnets of type VACODYM VD745HR which offer highest remanence values and thus energy densities currently available. The excellent magnetic properties of this material group can be traced to the strongly magnetic matrix phase Nd₂Fe₁₄B featuring very high saturation polarization and high magnetic anisotropy. Each two of the four magnets are facing each other leaving an air gap with

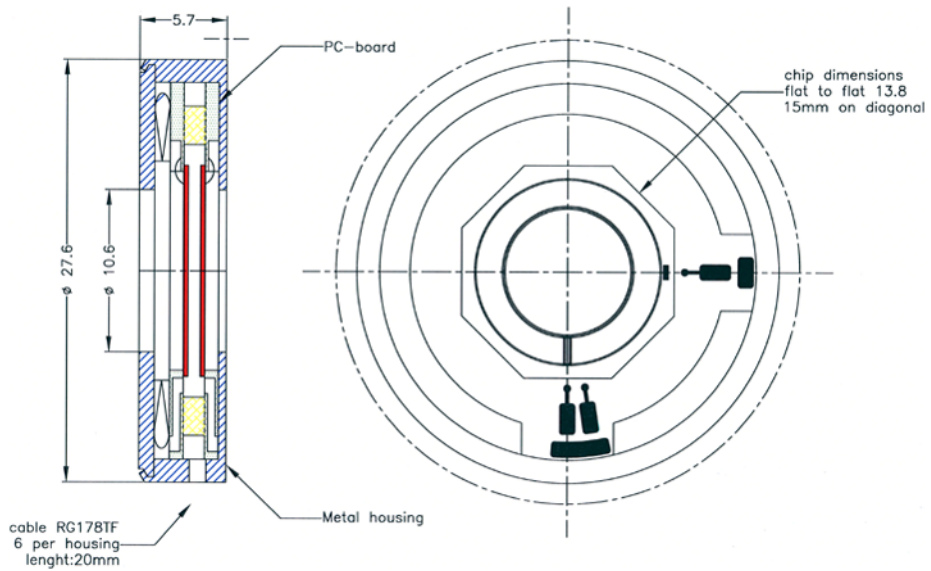


Fig. 3 Passivated ion-implanted planar silicon (PIPS) detector layout (Canberra, Belgium)

the necessary magnetic induction to deflect the electrons. Two yokes, made of the iron–cobalt alloy VACOFLEX 50, combine the two sets intensifying the magnetic induction. The long-range field is attenuated by having two oppositely polarized magnetic dipoles at close distance. Thus, the two air gaps provided by the magnet system serve two sensor systems simultaneously with anti-parallel viewing directions at minimum weight penalty while satisfying the stringent requirements on magnetic cleanliness.

A number of design options were investigated for the magnet system the most significant of which were an evaluation of the magnetic field strength and homogeneity in the air gaps. Both finite-element field calculations and an analytical approximation yield a maximum magnetic induction of 500 mT in the center of the air gap decaying to 170 mT towards the edges. A large number of magnets were fabricated and precisely measured to allow selection of individual magnets according to minimum differences in remanence and polarization vector. Thus the magnet manufacturer (Vacuumschmelze, Germany) could reduce the mismatch to better than 0.5%. The far-field as measured with the magnetometer of the MAG instrument onboard STEREO amounted to 1.8 nT at a distance of 3 m.

3.1.5 The Absorption Foil

The requirements on the absorber are demanding: while ultrathin, it must feature thermal stability over a large temperature range, a high physical strength against pressure differential and micrometeoroid impact, low sensitivity to thermal cycling and creep, high stability against exposure to UV and particle radiation, and low outgassing characteristics. The material of choice is Parylene N, a thin polymer film membrane which will stop about 400 keV protons with a corresponding range of $5.7 \times 10^{-4} \text{ g/cm}^2$ in plastic. While the exact foil thickness is not critical, the homogeneity is. The Parylene N pellicle with a specific gravity of 1.12 g/cm^3 has a measured uniform thickness of $4.95 \mu\text{m}$ with an amazingly small variation of $\pm 0.2 \mu\text{m}$ over the diameter of 3 cm. A 100 nm Al coating is evaporated on both sides of the pellicles.

3.2 The Onboard Electronics

Two identical electronics units are mounted close to their respective telescopes. Each electronics unit analyses the signals of four SSDs and four associated guard rings. One Particle Detector Front End (PDFE) integrated circuit is used to analyze the charge pulse from detector D1, using its guard ring in anti-coincidence. A second PDFE is used to analyze the signal from D2 in anti-coincidence with its guard ring. Furthermore, anti-coincidence signals between D1 and D2 ensure that an “exclusive OR” function is performed, i.e. only stopping particles are analyzed. In a special calibration mode, this exclusive OR is inhibited in order to use minimum ionizing particles for on-station calibration. The signals from the detector pairs D3/D4 through D7/D8 are treated in an identical fashion.

Additional 10 housekeeping signals are sampled, digitized, and transferred to the SEP-Central processor to monitor SEPT health and status. A specific test pulse generator permits a functional check-out of the instrument in flight and during ground testing. The low-level operation of SEPT electronics is controlled by a specific FPGA. The high level operation of SEPT is controlled by the SEP-Central processor by way of commands sent on the serial interface. The same serial interface is used to transfer all scientific, calibration and housekeeping data from SEPT to the SEP-Central processor. The block diagram in Fig. 4 shows in some more detail the front-end electronics for one of the two SEPT telescopes, together with the accumulation logic. Figure 5 shows top and bottom views of the electronics package.

3.2.1 PDFE

The Particle Detector Front End (PDFE) is a custom design Application Specific Integrated Circuit (ASIC) using a standard 0.7 μm CMOS process suited for charged particle spectroscopy applications which has been developed for the European Space Agency (ESA) by KU Leuven/Belgium and IMEC-InVomec/Belgium (Wouters et al. 2000). A block diagram is shown in Fig. 6. It contains two analog charge-amplifying channels. The first channel is the main one; the second channel is used for coincidence or gating purposes. The coincidence detection can also be done externally via a digital input. Eight-bit-programmable discriminators are provided for both channels. For the main channel, after peak detection, an 8-bit analog to digital conversion is performed. It can be cascaded together with more PDFEs to control a multiple detector telescope. The operation of the PDFE is controlled via pins and a serial interface which permits also uploading of parameters. The PDFE features are given in Table 6.

3.2.2 FPGA

The Field Programmable Gate Array (FPGA) controls operations of the SEPT electronics. It steers the operation of the four PDFEs, reads their conversion results, applies logarithmic binning (selectable) to the data, reads, increments, and stores counter contents kept in the SRAM. It handles the communication interface with the SEP-Central processor, i.e. data transmission, command receipt and command interpretation. It controls the test generator and housekeeping multiplexer.

Upon detection of a valid event, the PDFE notifies the FPGA which reads the parallel output of the PDFE. Dependent on mode selection the address compressor either does a quasi-logarithmic or linear binning. The result is used as an address in the SRAM where the corresponding 24-bit counter is incremented. A timing command from the SEP-Central processor causes the FPGA to transfer the accumulated data: either 8 histograms with 32 bins of 24-bit

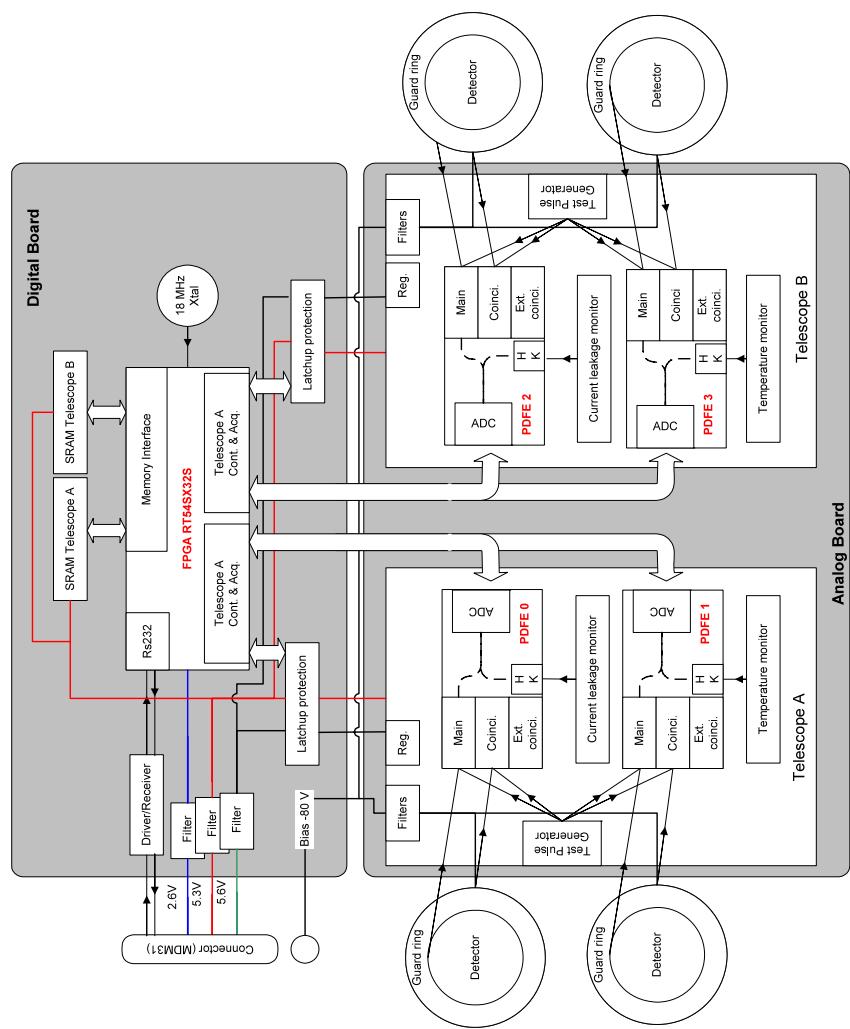


Fig. 4 SEPT electronics block diagram

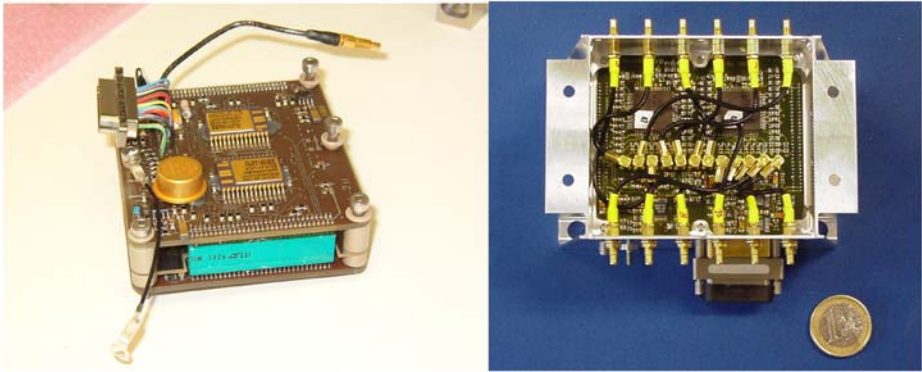


Fig. 5 Electronics board stack (*left*) and top view of analog board (*right*)

Table 6 PDFE specifications

Charge amplifying channels	1. main channel with shaper, baseline restorer, peak detector sample/hold 2. (anti-) coincidence channel for gating
Discriminators	1. 8-bit programmable for main channel 2. 8-bit programmable for coin. channel
Analog-to-digital converter	Linear 8-bit ADC
Operation	Completely event-driven
Radiation protection	All internal registers SEE (single event effects) protected
Package	64 pin CQFP (Ceramic Quad Flat pack)
Maximum detector capacitance	100 pF
Minimum/maximum detection charge	0.37/100 fC (8.8 keV / 2.3 MeV)
Conversion gain	30 mV/fC
Conversion gain adjustment	$\pm 5\%$
Noise	
at 0 pF detector capacitance	740 e_{rms} or 6.3 keV FWHM (measured)
at 120 pF	1160 e_{rms} or 9.8 keV FWHM (measured)
Noise slope	4.2 e_{rms}/pF (30 eV/pF)
Peaking time	1 μs
Maximum counting rate at	
maximum detection charge	25 kSamples/s
maximum detection charge/40	250 kSamples/s
Maximum pulse amplitude at analog output	3 V

depth (logarithmic binning) or 8 histograms with 256 bins of 24-bit depth (linear binning). Linear binning is only used on unit level during ground checkout. After the transfer, the counters are reset.

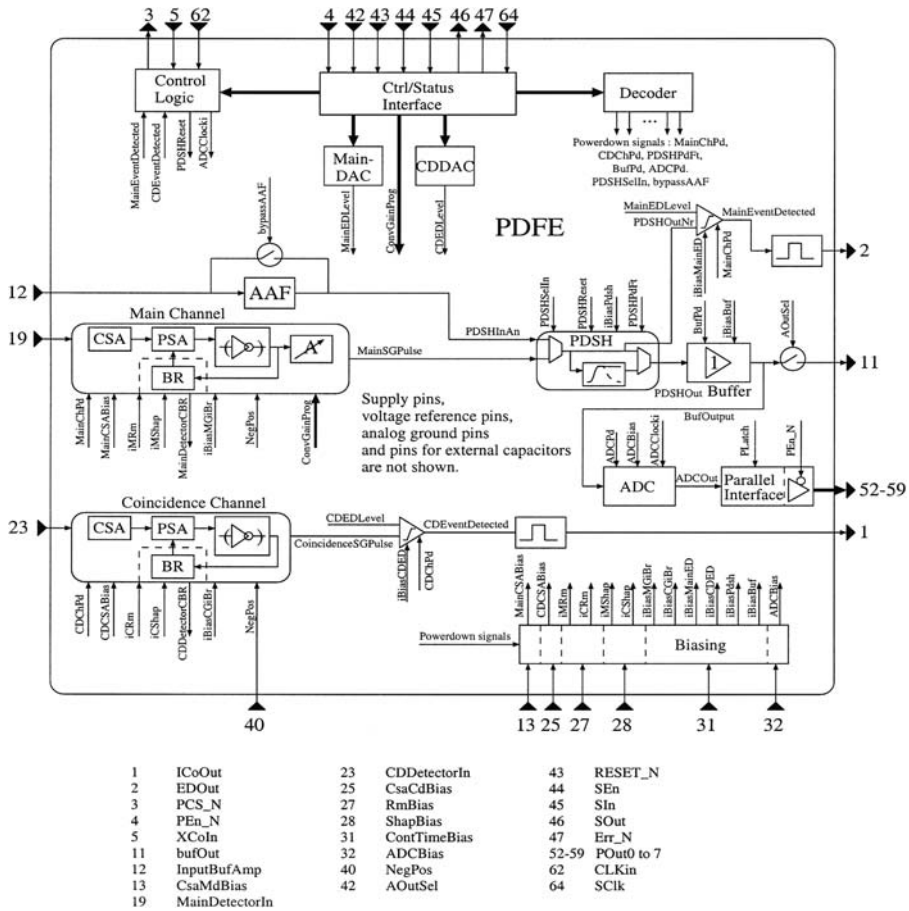


Fig. 6 PDFE block diagram

On command the FPGA can start the test pulse generator which feeds pulses of 4 different amplitudes to the 8 test inputs of the 4 PDFEs. A 4-bit mask defines the set of inputs for coincidence/anti-coincidence verification. Upon completion the generator is automatically switched off returning SEPT into nominal operation mode. Also on command, the FPGA can transfer to the SEP-Central processor the 10 housekeeping channels (2 temperatures and 8 detector leakage currents), which were converted by the PDFE internal ADC.

As the PDFE may develop latch-ups, the supply lines for the PDFE need to be current limited and—in case of a latch-up trigger—to be power cycled. This is to remove the latch-up condition from the chip. When sensing over-current conditions on the analog or digital supply lines, the latch-up monitor automatically switches off the corresponding telescope. A 900 μ s built-in timer is used to filter spurious signals. When power is reapplied normal operation can be resumed.

The ACTEL RT54SX32S FPGA is fed by an 18 MHz crystal oscillator from which the core 4.5 MHz clock is derived as well as a hybrid 4 MHz clock used for each PDFE. The verification of the FPGA design has been performed using the initial register transfer level

VHDL model and dedicated test benches. The FPGA design and verification was carried out by Gaisler Research (Sweden) under ESA contract.

3.2.3 Coincidence Logic

The coincidence logic is partly implemented in the PDFE and partly in the FPGA. The FPGA receives the four discriminator output signals and returns a separate coincidence signal to each PDFE. The PDFE can be configured to either ignore this external signal and use the discriminator output of its guard channel instead, or use the external coincidence signal requiring either coincidence or anti-coincidence. Table 7 summarizes the subset of useful combinations.

3.3 SEPT Telemetry Products

The scientific data from the two telescopes SEPT-E and SEPT-NS are comprised in a total of 8 histograms with 32 bins each. Four electron histograms (one for each of four directions) cover the electron energy range from 30 keV to 400 keV with quasi-logarithmic binning. Four proton histograms (one for each of four directions) cover the proton energy range from 60 keV to 2 MeV with quasi-logarithmic binning and a single bin for ions from 2–7 MeV/n. All histogram data are logarithmically compressed using a 24-bit to 14-bit compression scheme. Table 8 gives a summary.

Table 7 Coincidence filter configurations

FPGA filter mode (2 bit)	PDFE filter mode (3 bit)	Description	Operational mode
0	don't care	Disabled: no event is propagated	Nominal observation
1	4	Independent: no correlation with pair detector or guard	
2	4	Anti-coincidence with guard and pair and pair guard	
2	5	Coincidence with guard or pair or pair guard	
3	4	Anti-coincidence with pair	Calibration
3	5	Coincidence with pair	

Table 8 SEPT bit rate requirement

Data item	Number of channels	Bits per channel	Total number of bits	Time resolution
Histogram	8×32	14	3 584	60 s
Single rate	16/8	24	48	8×60 s
Leakage current	16	8	128	60 s
Temperature	4	8	32	60 s
Status	2	168	336	60 s
Lookup table	2	96	192	60 s
Total			4 320	

Table 9 SEPT beacon mode data

Species	Energy window [keV]		Geom. factor [cm ² sr]
Electrons	35	65	4×0.13
Electrons	65	125	0.52
Electrons	125	255	0.52
Electrons	255	485	4×0.13
Ions (mostly protons)	75	137	4×0.17
Ions (mostly protons)	137	623	0.68
Ions (mostly protons)	623	2224	0.68
Ions (mostly protons)	2224	6500	4×0.17

To evaluate the detector health, 16 single detector rates (8 center disks, 8 guard rings, subcommutated by factor 8) and 16 bias leakage currents are monitored along with four telescope temperatures.

The total SEPT bit rate requirement including header and checksum but excluding analog housekeeping is 4352 bits per 60 seconds (2 science telemetry packets of length 272 bytes each) corresponding to 72.53 bits/s. Leakage currents and temperatures are included as a subset in the SEP housekeeping packets.

3.4 SEPT Beacon Mode Data

SEPT will provide electron and proton rates in four energy channels for each species for continuous transmission of beacon mode data to the ground station. The lowest and highest energy channels are sectorized in the four look directions while the two mid-range rates are summed over the four look directions. This results in a total of 20 rates shown in Table 9, which are compressed using a 24-to-16 bit compression scheme for transmission. The time resolution is 60 seconds.

3.5 SEPT Commands

The SEPT-E and -NS instruments are completely independent. They do not have their own command processors. Commanding for SEPT is received and executed by the SEP-Central processor. The command language is FORTH. The two instruments are powered on whenever the SEP-suite of instruments is commanded on. However, detector bias may be commanded off or on separately. Also, the two anti-parallel viewing telescopes within one instrument may be switched off separately to recover from a catastrophic failure. High level commands change the operational mode of the instruments. Low level commands change operational parameters. Some parameters can be changed only by variable assignment. Variable and command names given in Tables 10 and 11, respectively, are all uppercase. Lower-case letters in the tables denote: s = 1, 2 (S/C), i = E, N (instrument), p = 0, 1, 2, 3 (PDFE).

3.6 Mission Operations

The main concern for the SEPT sensors is solar heat input when the STEREO spacecraft is in off-nominal attitude. During the transfer trajectory phase, when the spacecraft is in a highly elliptical orbit (HEO), there is the possibility that the SEPT apertures will view

Table 10 SEPT variables

Variable	Default	Description	Related to
ACC-TIME	15 256	Accumulation time in 1/256 sec	
GAINp-i	\$80	PDFE mode and gain	SPFMs
MLEVp-i	15	PDFE main threshold	MLEV-i!
CLEVP-i	20	PDFE guard threshold	CLEV-i!
ELEC-BINn	1, 4, 8, 13, 18	Beacon electron energy bins, $n = 1, \dots, 5$	
ION-BINn	1, 7, 20, 31, 32	Beacon proton energy bins, $n = 1, \dots, 5$	
SPiCAL-N	\$AA	Coincidence filter mode, nominal	
SPiCAL-C	\$FF	Coincidence filter mode, calibration	SPiCALM
SPi-SEQL	40	Duration of test runs in minutes	SPiCALM, SPiTEST
SPi-PAGE	0	Memory page	
SPi-TGOAL	152	Op-heater temperature goal, degC + 166	SPi-HAUTF
SPi-TPARM	256	Op-heater scaling parameter	SPi-HAUTF
SPi-HAUTF	-1	Op-heater regulator enable flag	
SPi-TPREF	0	Preferred temperature sensor (0 = A, 1 = B)	SPi-HAUTF
SPiAT-EN	-1	Enable use of temperature sensor A	SPi-TPREF
SPiBT-EN	-1	Enable use of temperature sensor B	SPi-TPREF
SPi-SHLVL	2	Heater level while no temps available	
SPi-MHLVL	0	Manual heater level, 0, ..., 10	SPi-HAUTF
SPFMs-INI	array[24]	S/C-s PDFE configuration table	SPFMs
SING-NORM	0, 4, 1, 5, 2, 6, 3, 7	Nominal single counter address table	
SING-TEST	array[40]	Test mode single counter address table	SPiTEST
CALCONF	array[40]	Test pulser configuration table	SPiTEST
FLTRMODE	array[40]	Test mode coincidence filter modes	SPiTEST
PDFEMODE	array[40]	Test mode PDFE mode and gain	SPiTEST

the Sun for periods of about 20 minutes. The thermal input is a hazard to the solid state detectors, to the magnet, and to the foil. Owing to the low energy thresholds no aperture foils are built in for the proton telescopes, and the foil thickness of the electron telescopes is exactly determined in terms of stopping power for protons and cannot be adjusted for optimum thermal control. Hence, in space, direct sunlight as well as specular straylight must be avoided and diffuse straylight minimized to guarantee flawless detector performance. All four telescope apertures are equipped with doors which will be opened by one-shot cover release mechanisms once HEO phase is passed on mission day 54 and 89 for Behind and Ahead spacecraft, respectively.

Initial turn-on in space will occur 19 days after launch to allow for outgassing. Commissioning will take place following the cover release. Thereafter SEPT will operate autonomously without the need for ground intervention except for occasional (every few months) commanding into calibration mode. Discriminator thresholds will be adjusted by table upload if deemed necessary after commissioning. Further table uploads or change of

Table 11 SEPT commands

Command	Parameter	Description	Related to
SPiNORM		Nominal mode	
SPiAONLY		Telescope A only	
SPiBONLY		Telescope B only	
n SPiCALM	n: number of acquisitions	Calibration mode	
n SPiTEST	n: number of acquisitions	Test pulse mode	
SPiOFF		Turn off	
SAUTO-ON		Automatic latchup mode	
SAUTO-OFF		Automatic latchup mode off	
SPFMs!		Load default PDFE configuration	SPFMs-INI
SP-GO		Turn on Bias, nominal mode	
SPFMs-GO		SPFMs! SP-GO	
n MLEV-i!	n: threshold	Load all main thresholds	MLEVp-i
n CLEV-i!	n: threshold	Load all guard thresholds	CLEVp-i
SP-SAVE		Save all main thresholds	MLEVp-i
SP-RESTORE		Restore main thresholds	SP-SAVE

coincidence filter configuration will only be commanded to compensate for noisy detectors or other anomalies.

3.7 Mechanical and Thermal Design

The sensor and electronics box housing are using a weight-saving design with a wall thickness of 1 mm aluminium. An Alodine 1200 protective coating, also known as Iridite or Chromate Conversion, is applied for desired electrical resistance characteristics. The detector stacks are mounted in their own Ni-plated Al housings with Delrin spacers and glued on FR4 frames with EPO-TEK electrically conductive adhesive with matching thermal expansion coefficients. Contact to ohmic and junction sides is made by wire-bonding.

The instruments will be mostly covered by MLI thermal blankets except for the apertures and doors. Once open in space, the doors will be illuminated by sunlight. To mitigate heat input into the telescopes, the doors, hinges and hinge-bolts are made of titanium for its lower heat conductance. The titanium parts received an anodizing treatment with Teflon impregnation to prevent fretting or cold welding.

Those parts of the collimators which receive sunlight are covered with Goddard Composite. The sides of the electronics box facing away from the Sun are covered with silver-coated Teflon to create radiator surfaces. The instruments are mounted on the spacecraft thermally isolated via Ultem bushings. Both operational and survival heaters are provided for thermal control. The nominal internal operating temperature is in the range -10 to $+20^{\circ}\text{C}$. Black anodizing is used on inside surfaces for better radiative coupling. Chemglaze Z306 on the magnets and magnet mount will absorb any stray-light.

The two doors on each side share a Shape Memory Alloy (SMA) activated pin-puller developed under NASA contract. A titanium rod attached to the pin-puller shaft transmits the pin-puller action to the door clevises.

SEPT uses a simple purging system to allow dry nitrogen purge of the SSDs during ground operations and storage until some time into the launch campaign. The purge inlet

is integrated into the side support of the sensor and consists of a purge barb with a flow restrictor. A light-tight purge path is machined into the detector housing, detector mounting frame, and magnet mount to allow free diffusion of the purge gas. No outlet is necessary, the proton aperture is essentially open as the doors are not hermetically sealing. The electronics box is not purged, but evacuation vents are designed in for launch.

3.8 Electrical GSE

The SEPT EGSE consists of a power controller box and a core software running on a dedicated desktop, both connected via RS232 interface. One EGSE can provide the voltage rails (2.6 volt digital, 5.3 volt digital, 5.6 volt analog and -80 volt bias) for two SEPT units. The control software on the desktop was written in visual C/C++, it features a graphical interface for configuration and data display as well as data logging and scripting capabilities (Vbscript) used extensively during environmental tests. The EGSE was developed in a collaboration between the KTH Alfvén Laboratory (Sweden) and ESA/ESTEC.

4 Calibrations and Performance

4.1 Electronic Calibration

The SEPT electronics was tested without detectors in order to establish an intercalibration of all analog channels with an external precision pulse generator, to map out the discriminator thresholds, to measure the differential non-linearity (DNL), and to calibrate the leakage current monitor. Figure 7 shows an example revealing a 2^4 pattern in DNL. SEPT data plots with full 256 channel resolution in the following sections were corrected for the effects of DNL. These measurements were performed on all SEPT flight instruments and the flight spare.

4.2 Source Tests

The 16 detectors making up the eight stacks of the four SEPT instruments were selected from a total of 30 SSD devices supplied by the detector manufacturer. Each individual detector was calibrated with conversion electrons from radioactive sources ^{109}Cd , ^{133}Ba , and ^{207}Bi .

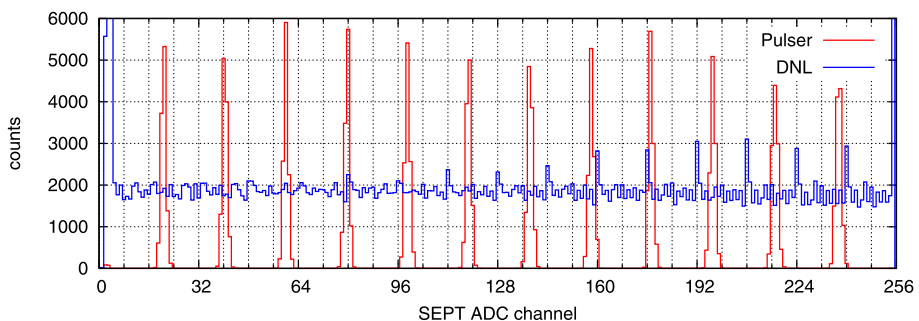


Fig. 7 Electronics calibration with an external precision pulse generator. *Red*: intercalibration with reproducible pulse amplitudes. *Blue*: linear amplitude ramp for differential non-linearity (DNL) measurement

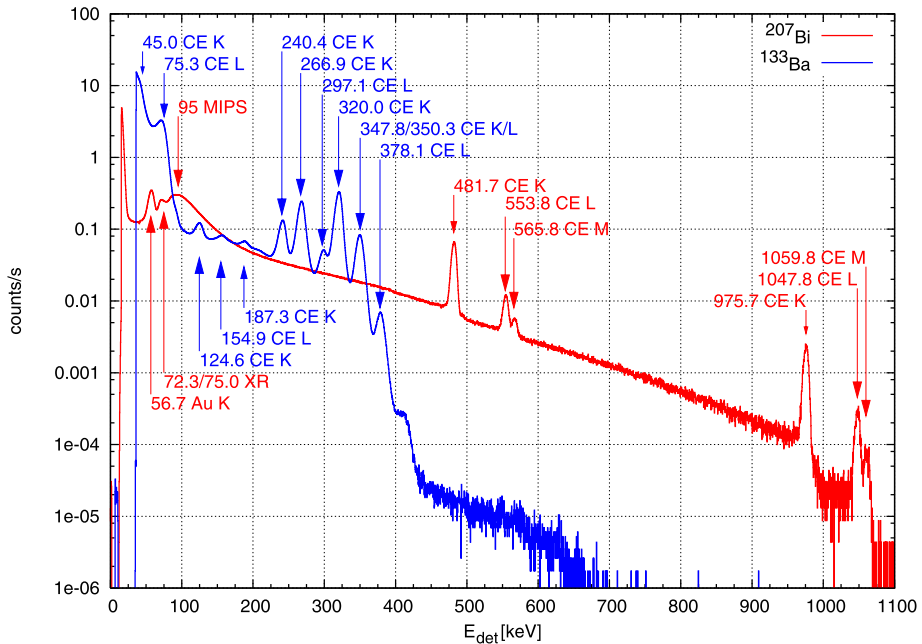


Fig. 8 Silicon detector response to conversion electrons (CE) from ^{207}Bi (red) and ^{133}Ba (blue) sources, measured with laboratory electronics. K, L, and M shell energies can be resolved

The sample spectra of ^{133}Ba and ^{207}Bi in Fig. 8 were measured in vacuum with laboratory electronics, demonstrating an energy resolution of the detectors of 7 keV FWHM.

Measurements with the integrated telescopes using the onboard electronics in linear mode (256 channels, see Fig. 9) give an energy resolution of 25 keV FWHM. Note that the onboard quasi-logarithmic binning which was introduced to conserve bitrate will further reduce the energy resolution above 100 keV. These measurements were performed in air, but energy loss through ionisation in the source (^{133}Ba sealed between plastic foils 0.1 mm and 0.015 mm thick, ^{207}Bi sealed between Mylar foils 0.9 mg/cm² thick) and in 2 cm air have been appropriately taken into account.

The blue graph in Fig. 9 is the direct signal of the conversion electrons in the electron detector, measured in anti-coincidence mode. The orange graph is the signal from penetrating electrons in the pair proton detector, measured in coincidence. The black graph is the Compton scattering signal from gamma-radiation lines in the neighbouring telescope, which is shielded from the electron radiation by the sensor housing. The magenta graph shows a measurement with the source placed in front of a proton telescope aperture, where the conversion electron signal is reduced and the 482 keV lines are not visible at all due to the deflection in the magnetic field. Finally, the red graph is the SEPT response to atmospheric muons from cosmic radiation. Both the top and bottom x-axis show the energy in keV, but the tic marks on the top show the telemetry data binning in 32 bins.

The dominant electron lines from the ^{207}Bi source, at 481 and 975 keV, were used to measure the end-to-end gain of all electron telescopes. Figure 10 shows a measurement with a ^{133}Ba source, which provides an additional calibration point in the lower energy range. The best estimate of the offset of the ADC, being 10 keV at the center of ADC channel zero, was derived from this measurement. The external pulser measurements from Fig. 7 were used to

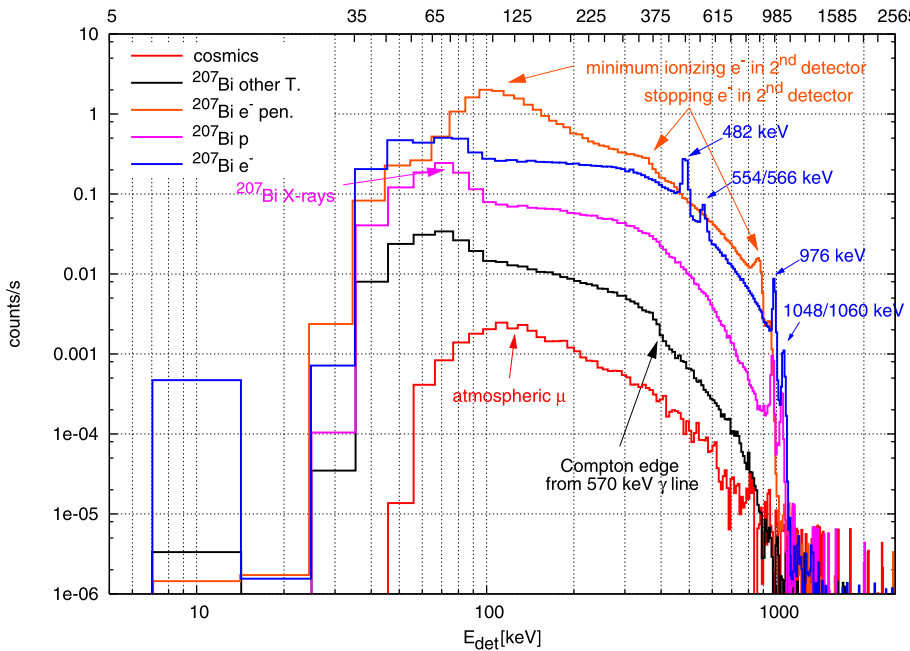


Fig. 9 SEPT response to the radiation field of a ^{207}Bi source placed in front of an electron (blue) and a proton (magenta) telescope. See text for details

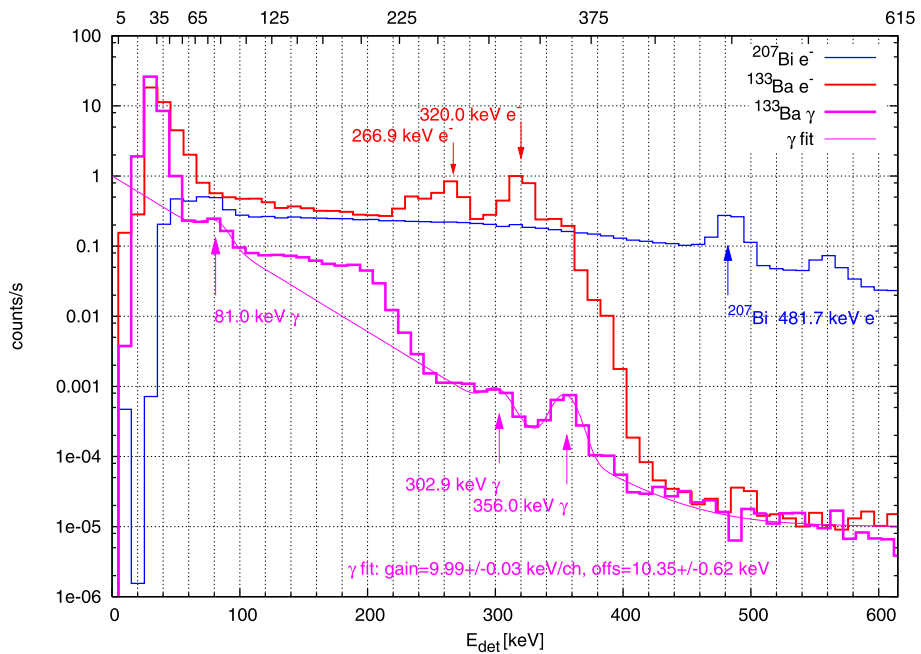


Fig. 10 SEPT response to conversion electrons (red) and γ -ray lines (magenta) from a ^{133}Ba source

intercalibrate all telescopes. From these results a set of gain correction factors is derived to adjust each telescope to a gain of 10 keV/ADC channel. These corrections will be included in the SEP-Central flight software tables and loaded into the PDFE registers before each data acquisition cycle.

4.3 Accelerator Calibration

The SEPT flight spare was calibrated at the Physikalisch-Technische Bundesanstalt (PTB) in Braunschweig, Germany, in February, 2006 with proton and alpha particles from the 3.75 MV Van-de-Graaff accelerator and from the 17 MeV cyclotron TCC-CV28 at various beam energies. These measurements were used to calibrate and check the performance of several instrument functions, including: detector thresholds, detection efficiency, coincidence/anti-coincidence logic, ADC response, counting rates, saturation effects in a high rate environment, accuracy of the range-energy relation for the absorption foil, dead layer, and front detector. Only the flight spare was calibrated at the accelerators, but the spare telescope is representative enough that the results are applicable also to the flight units. In these calibrations, the flight spare was mounted in a vacuum chamber to avoid beam degradation in air at low energies. The particle beams were injected along the boresight direction of both the electron and the proton apertures.

The telescope response for protons is shown in Fig. 11 and for alphas in Fig. 12.

Plotting the detected energy in the telescope on a scale determined by the conversion electron measurements versus the beam energy determined by the accelerator facility's calibration magnets, we can see the effects of detector dead layers affecting the ions at low energies, see Fig. 13.

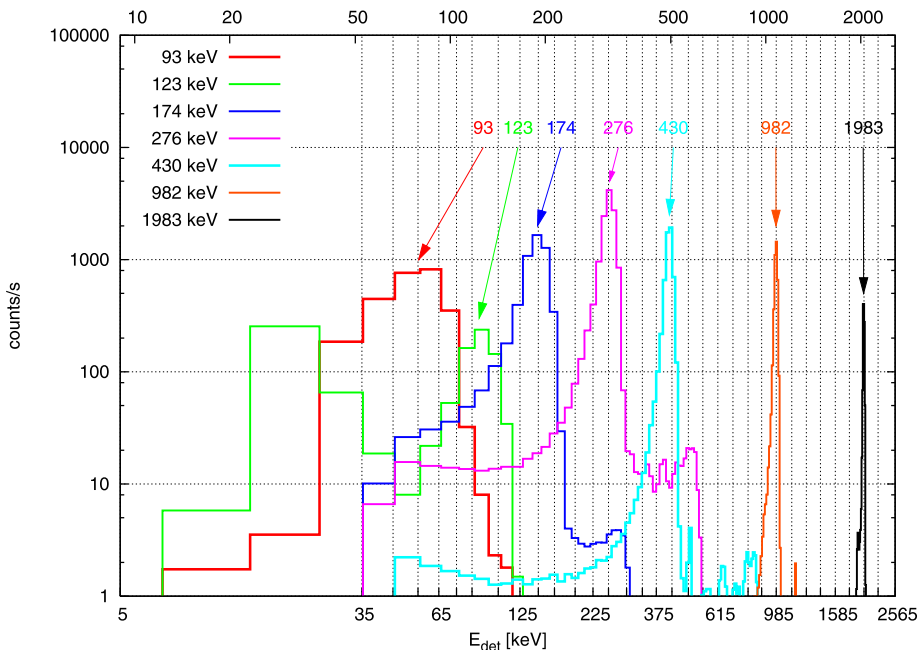


Fig. 11 SEPT response to monoenergetic proton beams at PTB. The *bottom* *x*-axis tic marks show the telemetry binning

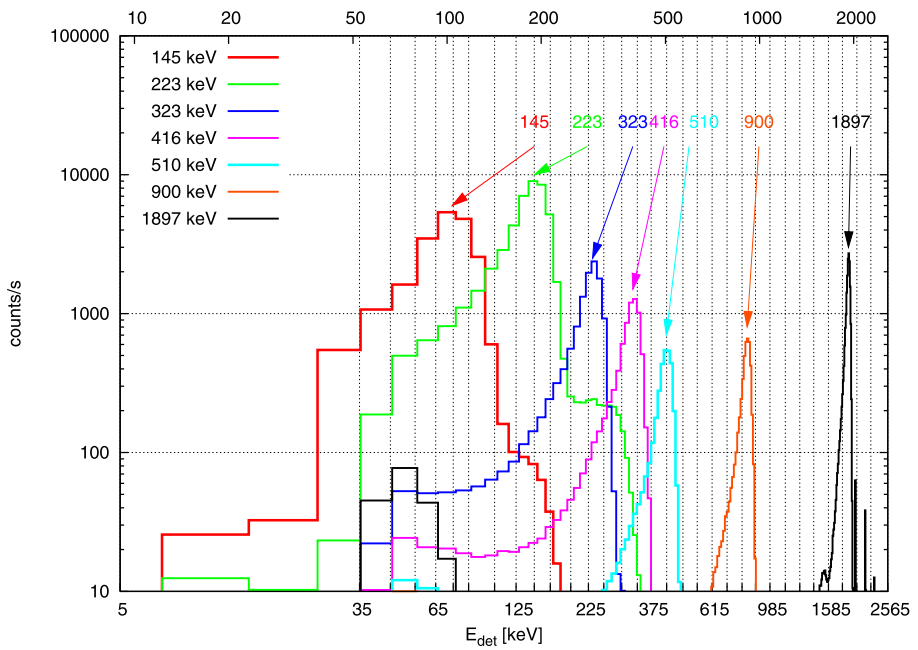


Fig. 12 SEPT response to monoenergetic alpha particle beams at PTB. The *bottom* x-axis tic marks show the telemetry binning

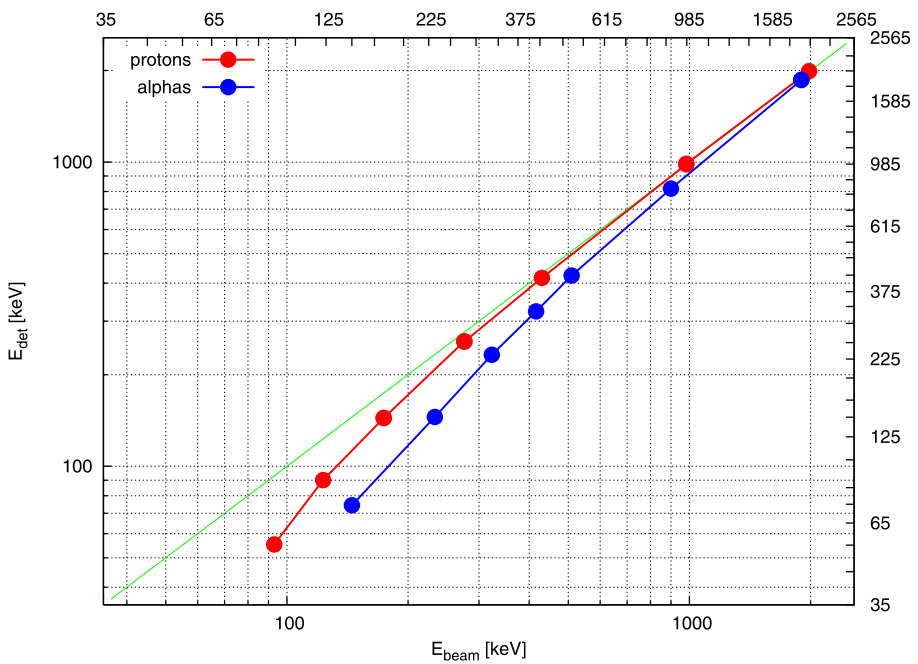


Fig. 13 Proton and alpha particle calibration on the electron energy scale

Table 12 SEPT energy bins for electrons, protons and alpha particles (values are upper boundaries of energy bins)

Bin	ADC	Electrons	Protons	Alphas
0	2	35 keV	75 keV	96 keV
1	3	45 keV	84 keV	108 keV
2	4	55 keV	93 keV	121 keV
3	5	65 keV	101 keV	133 keV
4	6	75 keV	110 keV	146 keV
5	7	85 keV	119 keV	158 keV
6	9	105 keV	137 keV	183 keV
7	11	125 keV	156 keV	208 keV
8	13	145 keV	175 keV	233 keV
9	15	165 keV	193 keV	253 keV
10	18	195 keV	220 keV	284 keV
11	21	225 keV	246 keV	315 keV
12	24	255 keV	273 keV	346 keV
13	28	295 keV	312 keV	387 keV
14	32	335 keV	351 keV	427 keV
15	36	375 keV	390 keV	464 keV
16	41	425 keV	438 keV	511 keV
17	47	485 keV	496 keV	570 keV
18	53	545 keV	555 keV	629 keV
19	60	615 keV	623 keV	698 keV
20	68	695 keV	701 keV	777 keV
21	77	785 keV	788 keV	866 keV
22	86	875 keV	876 keV	953 keV
23	97	985 keV	983 keV	1058 keV
24	110	1 115 keV	1 112 keV	1 183 keV
25	124	1 255 keV	1 251 keV	1 316 keV
26	139	1 405 keV	1 400 keV	1 459 keV
27	157	1 585 keV	1 578 keV	1 631 keV
28	176	1 775 keV	1 767 keV	1 812 keV
29	198	1 995 keV	1 985 keV	2 022 keV
30	222	2 235 keV	2 224 keV	2 251 keV

The accelerator measurements, together with the adjusted electron gains, lead to the SEPT energy bin table shown in Table 12. The table lists the upper boundary of the energy bins. The first bin (bin 0) will be dominated by background counts. The programmable discriminator thresholds will be set in-flight by telecommand to achieve a tolerable background level. Hence the detection efficiency of the first bin will be less than 100% making this bin useful only when count rates are high. The last bin (bin 31) is not shown, it registers all ions above 2.25 MeV which stop in the front detector, mainly protons up to 6.5 MeV and alphas up to 26 MeV total energy. Due to limitations of storage capacity in the FPGA, only one binning table for the quasi-logarithmic binning could be made available for both elec-

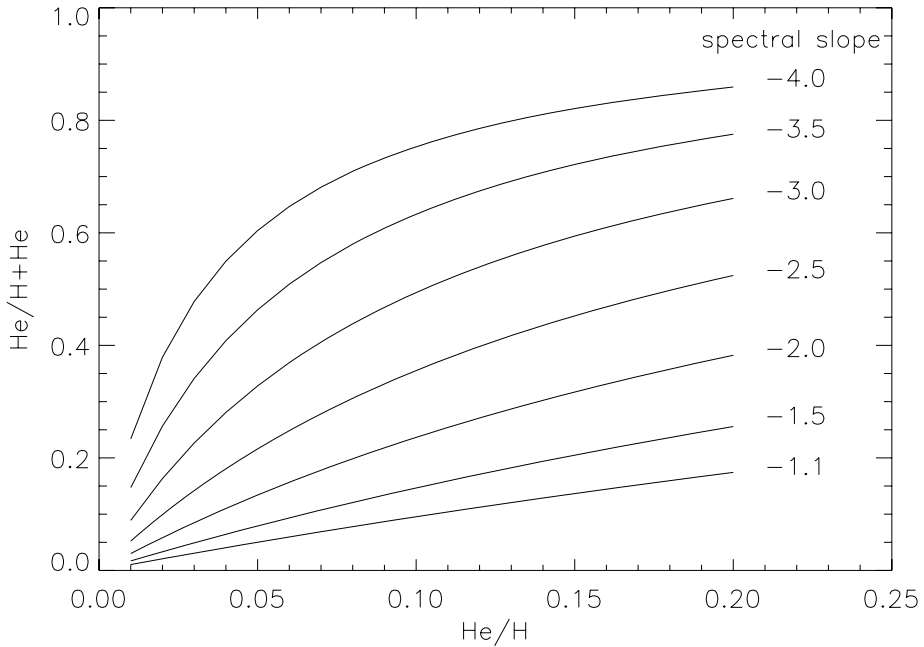


Fig. 14 Helium contribution to SEPT ion channels as a function of the helium to proton ratio typically observed in SEP events with spectral slopes as parameters

tron and proton energy measurements. Hence electron energies from 35 through 485 keV are mapped to histogram bins 1 through 17 only.

4.4 Response to Alpha Particles

In telescopes such as SEPT that measure the total energy of the ion, but not its nuclear charge, most of the response is usually due to protons, with smaller contributions due to helium and negligible contributions due to heavier nuclei. In most cases this is a good approximation, and the term “electron and proton telescope” is appropriate because helium and heavier ions can be safely neglected. However, in events where the spectra are steep or when the ratio He/H is enhanced, helium can account for a sizable amount of the ions against which SEPT cannot discriminate.

In order to derive the helium content in the ion channels we used the calibration results from Table 12, integrated over Bins 1 to 30, and plotted the $\text{He}/(\text{H} + \text{He})$ ratio versus the He/H ratio in a range typically observed for solar energetic particle events. Figure 14 shows the results with the spectral slopes as parameters assuming that H and He have the same spectral slope. While the He content is only 8% for a gradual event with a hard energy spectrum $\sim E^{-1.5}$ and low He/H ratio of 0.05, it can amount to 50% for an impulsive event with a steep spectrum ($\sim E^{-3}$) and large He/H ratio of 0.1.

4.5 In-Flight Test and Calibration

A simple in-flight test pulse generator provides an electronic stimulation with four different pulse amplitudes at the charge sensitive amplifier inputs in order to check the

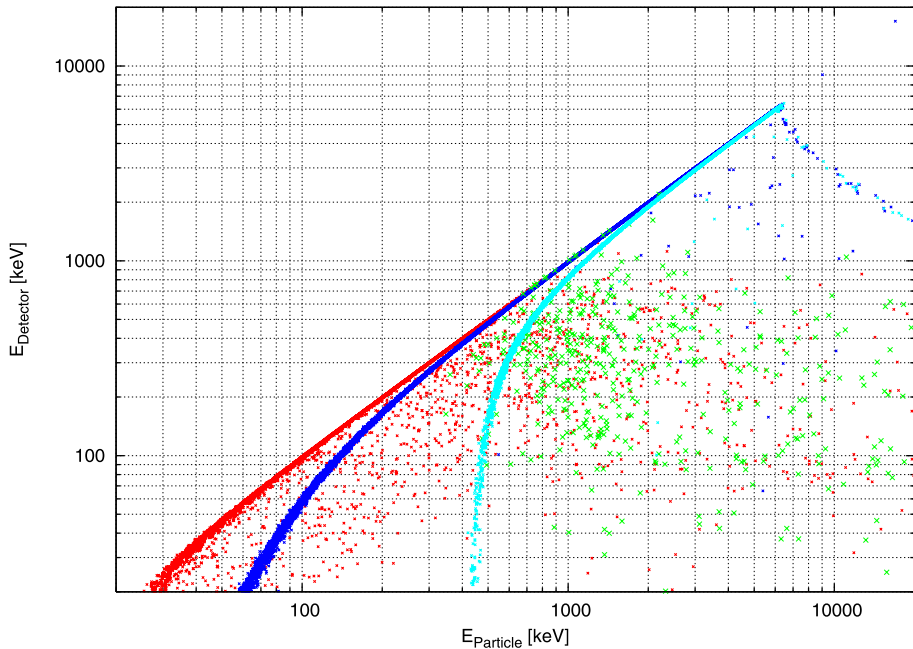


Fig. 15 SEPT response matrix from Geant4 Monte Carlo simulations. *Red* are electrons detected by the electron telescope. *Blue* are protons detected by the proton telescope. *Cyan* are protons detected as electrons, and *green* are electrons detected as protons

coincidence/anti-coincidence functionality and a coarse ADC response. Upon completion the generator is automatically switched off returning SEPT into nominal operation mode. While its accuracy is not sufficient to achieve an electronic calibration, SEPT can be calibrated using in-flight particles. To this end, the anti-coincidence condition between the two paired detectors can be commanded into coincidence to detect penetrating particles. The signals of minimum ionizing particles form a peak in the lower energy bins which can be used for on-station calibration.

4.6 Monte Carlo Simulation

A preliminary Monte Carlo model of the SEPT instrument was used to verify the design principle and to guide some design decisions, like the impact of a thicker detector window to guard against stray-light, and the choice of the foil material and thickness to stop protons.

Figure 15 shows the response matrix of the SEPT design, without taking into account detector and electronics noise. Shown on the y-axis is the energy deposited in the silicon detector volume versus the primary particle energy on the x-axis. A sharp threshold of 20 keV is assumed on the primary and all anti-coincidence detectors. While only a few electrons can mimic protons, the protons in a narrow energy range from 450 to 650 keV can mimic electrons and will have to be subtracted on ground knowing the well-measured proton spectrum in the neighbouring telescope.

Figure 16 shows the same data projected to the x-axis, scaled such that it will yield the geometry factor as a function of particle energy.

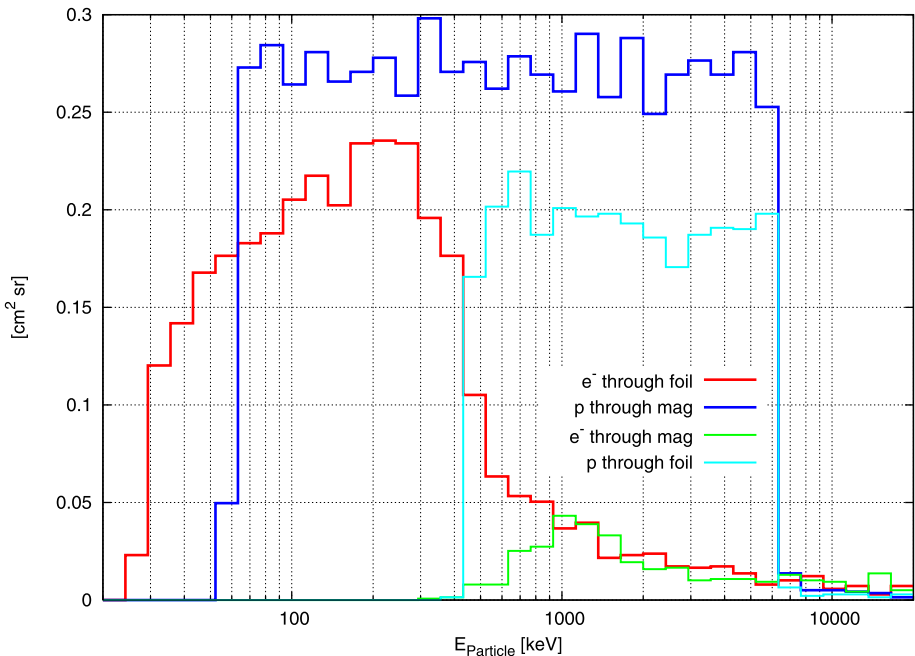


Fig. 16 SEPT geometry factor from Geant4 Monte Carlo simulations. *Red* are electrons detected by the electron telescope. *Blue* are protons detected by the proton telescope. *Cyan* are protons detected as electrons, and *green* are electrons detected as protons

Acknowledgements The efforts of R. Lin on the sensor design and of D. Curtis on the host of engineering issues during the development, manufacturing, test, and integration phases are gratefully acknowledged. We appreciate the professional workmanship of the contributions from all members of the IMPACT team. We acknowledge the support by P. Falkner on the electronics design and by S. Habinc on the FPGA design and manufacturing. Ion-implanted detectors were provided by Canberra Eurisys, special thanks to M. Keters and P. Burger. The magnet system was provided by Vacuumschmelze, special thanks to F. Jurisch. We also wish to express sincere thanks to all members of the teams in our home institutions who supported design and fabrication of the instruments, in particular in the areas of electrical and mechanical workmanship and engineering as well as administration. This work was partly supported by ‘Deutsches Zentrum für Luft- und Raumfahrt (DLR)’ under grant 50 OC 0004.

References

- H.V. Cane, R.E. McGuire, T.T. von Rosenvinge, *Astrophys. J.* **301**, 448 (1986)
- E.W. Cliver, in *High Energy Solar Physics*, ed. by R. Ramaty, N. Mandzhavidze, X.-M. Hua. American Institute of Physics Conf. Proc., vol. 374 (1996), p. 45
- C.M.S. Cohen et al., *Geophys. Res. Lett.* **26**, 2697 (1999)
- S.E. Forbush, *Phys. Rev.* **70**, 771 (1946)
- A. Galvin et al., *Space Sci. Rev.* (2007), this volume
- J.T. Gosling, D.N. Baker, S.J. Bame, W.C. Feldman, R.D. Zwickl, *J. Geophys. Res.* **92**, 8519 (1987)
- S.W. Kahler, in *High Energy Solar Physics*, ed. by R. Ramaty, N. Mandzhavidze, X.-M. Hua. American Institute of Physics Conf. Proc., vol. 374 (1996), p. 61
- M.-B. Kallenrode, *J. Phys. G Nucl. Phys.* **29**, 965 (2003)
- K.-L. Klein, A. Posner, *Astron. Astrophys.* **438**, 1029 (2005)
- B. Klecker et al., *Adv. Space Res.* (2006, in press)
- J. Luhmann et al. (2007), this volume, doi:[10.1007/s11214-007-9170-x](https://doi.org/10.1007/s11214-007-9170-x)

- A. Luhn, B. Klecker, D. Hovestadt, E. Moebius, *Astrophys. J.* **317**, 951 (1987)
G.M. Mason, J.E. Mazur, J.R. Dwyer, *Astrophys. J. Lett.* **525**, L133 (1999)
R.A. Mewaldt et al., *J. Geophys. Res.* **110**, A09S18 (2005)
R.A. Mewaldt et al. (2007), this volume
E. Moebius et al., *28th Internat. Cosmic Ray Conf.*, vol. 6 (2003), p. 3273
R. Mueller-Mellin, B. Heber, M.-B. Kallenrode, H. Kunow, G. Wibberenz, *Adv. Space Res.* **13**(6), 85 (1993)
P. Oakley, S. Krucker, R.P. Lin, American Astron. Society, SPD meeting #34, #16.7 (2003)
D.V. Reames, *Astrophys. J.* **330**, L71 (1988)
D.V. Reames, *Rev. Geophys. Suppl.* **585** (1995)
D.V. Reames, *Space Sci. Rev.* **90**, 413 (1999)
D.V. Reames, *Astrophys. J.* **571**, L63 (2002)
A.J. Tylka, P.R. Boberg, J.H. Adams Jr., L.P. Beahm, W.F. Dietrich, T. Kleis, *Astrophys. J.* **444**, L109 (1995)
T.T. von Rosenvinge et al. (2007), this volume
J. Wouters, S. Redant, K. Marent, C. Das, S. Habinc, B. Johlander, T. Sanderson, in *Proc. of the European Space Components Conferences ESCCON 2000*, 21–23 March 2000, ESTEC, Noordwijk, The Netherlands, ed. by B. Schürmann. European Space Agency, ESA-SP, vol. 439 (2000), p. 247